RSC Advances

ROYAL SOCIETY OF CHEMISTRY

www.rsc.org/advances

RSC Advances

Enhanced figure of merit in $Mg_2Si_{0.877}Ge_{0.1}Bi_{0.023}$/multi wall carbon nanotube nanocomposites

Nader Farahi,[a] Sagar Prabhudev,[b] Matthieu Bugnet,[b] Gianluigi A. Botton,[b] Jianbao Zhao,[c] John S. Tse,[c] James R. Salvador,[d] Holger Kleinke*[a]

[a] *Department of Chemistry and Waterloo Institute for Nanotechnology, University of Waterloo, Waterloo, ON, Canada N2L 3G1*

[b] *Materials Science and Engineering Department, McMaster University, Hamilton, ON, Canada L8S 4L8*

[c] *Department of Physics and Engineering Physics, University of Saskatchewan, Saskatoon, SK, Canada S7N 5B2*

[d] *General Motors Research & Development Center, Warren, MI, USA 48154*

The effect of multi wall carbon nanotubes (CNT) on the thermoelectric properties of $Mg_2Si_{0.877}Ge_{0.1}Bi_{0.023}$ was examined. While introducing CNTs increases the electrical conductivity from around 450 $\Omega^{-1}cm^{-1}$ to 500 $\Omega^{-1}cm^{-1}$ at 323 K, the increase is neutralized at higher temperature, with the conductivity resulting in 440 $\Omega^{-1}cm^{-1}$ - 470 $\Omega^{-1}cm^{-1}$ at 773 K. The Seebeck coefficient of all nanocomposites is enhanced at 773 K due to energy filtering that stems from the introduction of CNTs - $Mg_2Si_{0.877}Ge_{0.1}Bi_{0.023}$ interfaces. The combined effect of CNTs on both thermal and electrical conductivity leads to an approximately 20% power factor improvement, with the best sample reaching a maximum value of ~19 $\mu W\ cm^{-1}K^{-2}$ at 773 K. The lattice thermal conductivity of the nanocomposites is reduced due to the phonon scattering by nanodomains and grain, particularly at medium temperatures, resulting in a slight reduction in total thermal conductivity. According to high resolution transmission electron microscopy studies, bismuth is homogenously distributed within the grains, while germanium is accumulated at the grain boundaries. All in all, the enhanced thermoelectric figure of merit of 0.67 at 773 K for the sample containing 0.5 weight-% MWCNT as compared to 0.55 for the pristine sample, demonstrates the promising effect of CNTs on the thermoelectric properties of

$Mg_2Si_{0.877}Ge_{0.1}Bi_{0.023}$.

*: Corresponding author contact information: kleinke@uwaterloo.ca

Keywords: magnesium silicide, thermoelectric, nanocomposites, multi wall carbon nano tubes

1. Introduction

After the discovery of carbon nanotubes (CNT),[1] numerous studies have been performed to reveal the properties and behaviour of these materials. It is crucial not only to understand their capabilities, but also to be able to manipulate their properties towards the desired application. This manipulation can be done through surface functionalization,[2] chirality control[3] and managing the number of walls[4] for multi-wall carbon nanotubes (MWCNT). Since energy is one of the main concerns of our time, it is practical to profit from these modern materials to tackle the energy challenges, such as waste heat recovery. So far, thermoelectric (TE) materials are some of the best candidates for this purpose, due to their exceptional capability to convert waste heat into electricity. Like other newly developed technologies, the quest for increasing the efficiency while mitigating the cost and toxicity of TE materials is still ongoing. The efficiency of a thermoelectric material depends on its figure of merit $zT = \sigma S^2 T \kappa^{-1}$, where σ, κ, S and T represent electrical conductivity, thermal conductivity, Seebeck coefficient and absolute temperature, respectively.[5–7]

To enhance zT based on the above equation, the electrical conductivity and the Seebeck coefficient need to be increased while maintaining or reducing the thermal conductivity. Unfortunately these properties are entangled in such a way that simultaneous improvements are not always feasible, as for example both the electrical and the thermal conductivity increase with higher charge carrier concentration, while the Seebeck coefficient decreases. One of the strategies to overcome this issue is through embedding nanomaterials into the bulk matrix, which is known as "nano-inclusion".[8] The idea of having nanostructures is to reduce thermal conductivity through scattering mid- to long- wavelength phonons, and to sustain electrical conductivity while improving S via energy filtering of carriers.[8–10] Carbon nanotubes, due to their spectacular electronic properties, can be considered as potential candidates for nano-inclusions in thermoelectric materials.[11–15] Even though CNTs had a positive effect on the

thermoelectric properties of Bi_2Te_3[16] and $Bi_2(Se,Te)_3$[17] by achieving $zT \sim 1.5$ at 350 K as compared to $zT \sim 1$ for the sample without nanotubes, the presence of rare and toxic tellurium would not fulfill the criteria for large scale industrial applications, further the temperature at which these materials are most efficient are well below those of most targeted waste heat recovery applications.

The rationale for this work is to investigate the effect of CNTs on the thermoelectric properties of more cost effective and eco-friendly materials. Magnesium silicide based materials, in this regard, are conspicuous as next generation high efficiency TE materials that are suitable for auto industry applications.[18] Thus far, single-wall carbon nanohorns (SWCNH),[19] TiO_2[20] and Si nanoparticles[21] were studied as nano-inclusions in Mg_2Si materials. Embedding SWCNHs improved room temperature electrical conductivity of Bi doped Mg_2Si from around 3 $\Omega^{-1}cm^{-1}$ to 100 $\Omega^{-1}cm^{-1}$. An improvement by a factor of 10 was also observed in the electrical conductivity of the samples containing TiO_2. Unfortunately, the nano-inclusions were not as effective as tin[22] or germanium[23] solid solutions in reducing the thermal conductivity of Mg_2Si thermoelectrics. The lowest room temperature thermal conductivity of around 6 W $m^{-1}K^{-1}$ was achieved for Mg_2Si/Si nanocomposites, which is approximately twice that of a solid solution.[22] The lack of similar investigations of $Mg_2Si_{1-x}Ge_x$ solid solutions motivated this study.

2. Experimental section

$Mg_2Si_{0.877}Ge_{0.1}Bi_{0.023}$ samples were synthesized by mixing the elements in tantalum tubes, according to the stoichiometric ratios, in argon filled glove box. Mg chips (99.98%, Sigma Aldrich, 4-30 mesh), Si powder (99.9%, Alfa Aesar, -100 mesh), Ge pieces (99.9999+%, Alfa Aesar, $\leq$ 2 cm) and Bi granules (99.99%, Sigma Aldrich) were used for our synthesis. The tantalum tubes were sealed under argon with an arc melter, and put into silica tubes, which were then sealed under vacuum. The tubes were heated in a resistance furnace at 923 K for a week. To achieve pure products, the samples were ground prior to annealing at 1173 K for another week.

To examine the purity of the synthesized samples, an Inel powder X-ray diffractometer with Cu-$K\alpha_1$ radiation and a position sensitive detector was used. All samples were pure except for small traces of MgO (Figure S1), which is a common side product in Mg_2Si based compounds.[24,25] The powders were manually mixed and divided into four batches. Different amount of carbon nanotubes (Sigma-Aldrich, Carbon nanotube, multi-walled; >90% MWCNT

basis, outer diameter 10 - 15 nm, inner diameter 2 - 6 nm, length 0.1 - 10 μm) were then added to each batch and mixed for 3 to 5 minutes using a Fisher Scientific vortex mixer until no MWCNT agglomerations were detected.

To perform the physical property measurements, the mixtures were then hot pressed in an Ar atmosphere at 973 K under 56 MPa using an Oxy-Gon hot press. To reduce stress and strain on the pellets during cooling, the pressure was released after sintering. The pressed pellets had 12.7 mm diameter and 2 mm thickness. The thermal conductivity, κ, of the pressed pellets was calculated by measuring the thermal diffusivity, α, under Ar flow using Anter Flashline FL3000 thermal properties analyzer between 300 K and 800 K. The obtained thermal diffusivity values were then multiplied by the density, d, of the pellets, as measured via the Archimedes method, and the specific heat, C_p, of the compounds, as calculated from the Dulong-Petit approximation, to yield $\kappa = \alpha\, d\, C_p$. The obtained densities together with the calculated specific heat of all the samples are available in Table S1. Our previous measurements of the specific heat of $Mg_2Si_{0.977-x}Ge_xBi_{0.023}$ samples validated the accuracy of Dulong-Petit approximation for this system.[26] Since adding CNT only changed the Dulong-Petit value of C_p by 2%, within the error range of the measurement, the calculated values were used to obtain the thermal conductivity.

The pressed pellets were thereafter cut into rectangular bars with the dimensions of approximately 12 × 2 × 2 mm^3, the electrical conductivity (σ) and Seebeck coefficient (S) measurements were carried out under helium atmosphere between 300 K and 800 K by using the ULVAC-RIKO ZEM-3 apparatus. Hall effect measurements where performed using a cryostat equipped with a 5 T magnet and with a Linear Research AC resistance bridge. Hall resistance values were measured from –3 T to 3 T from 5 K to 300 K. The carrier concentration (n) was calculated from the Hall coefficient, R_H, using the relationship $n = R_H^{-1}e^{-1}$, where e is the fundamental charge.

To verify the existence and examine the distribution of nanotubes within the samples at the micron level, scanning electron microscopy (SEM) analysis was performed on parts of selected pressed pellets (Figure S2) using a Zeiss ULTRA electron microscope associated with an EDX device, EDAX Pegasus 1200.

2.1. Transmission electron microscopy

Atomic-scale structural characterization and elemental analyses were performed using high

angle annular dark field imaging (HAADF) and energy dispersive X-ray spectroscopy (XEDS) in an aberration corrected scanning transmission electron microscope (STEM). STEM-HAADF employs a raster scanning electron probe to collect electrons that are elastically scattered at high angles. Upon converging the electron beam into a sub-angstrom probe, an atomic-scale image of materials is possible. The HAADF detector is designed in an annular geometry and placed in a diffraction plane below the sample so as to collect electrons emerging from the specimen at high scattering angles. Since the intensity of these high-angle scattered electrons is directly related to the atomic number of scattering atoms, the resulting image provides an atomic number (Z) contrast with intensities proportional to $Z^{1.6}$. In the case of the Mg_2Si sample doped with Ge and Bi, the atomic columns containing Ge (Z = 32) and Bi (Z = 83) are expected to appear significantly brighter compared to those of Mg (Z = 12) and Si (Z = 14). Further, the EDX elemental mapping and line profiles were based on Mg-K, Si-K, Ge-K and Bi-L spectral lines. Both of these analyses were performed on a FEI-Titan cubed microscope equipped with two hexapole-design spherical aberration correctors of the probe and image forming lenses, operated at 300 kV. The sample was thinned down to electron transparency by the wedge-polishing technique using a multiprep apparatus (Allied Inc.), and further argon ion milled using a Gentle Mill (Technoord Linda Inc.).

2.2. Raman spectroscopy

Dispersive Raman microscope (Renishaw Invia Raman Microscope) equipped with a Fourier transform infrared (FTIR) detector for sequential analysis at the same spot was used to measure pure multi-wall carbon nanotube and $Mg_2Si_{0.877}Ge_{0.1}Bi_{0.023}$ samples with additions of 0.5%, 1%, and 1.5% weight-% MWCNTs. The Raman spectroscopy was operated with a 514 nm argon ion laser (Modu-Laser Stellar Pro laser) and a 1800 line/mm grating. The laser power used was 10%, yielding 0.36 mW at the sample. The laser was focus on the flatten powder sample using a 20× objective, and the Raman signal was collected at 10 s. The measurement was calibrated by using Si (110), which was measured at 520 cm^{-1}. Data processing and analysis were accomplished using software Wire 3.4 (Renishaw, Inc.). The collection wave number range for Raman spectrum was from 100 cm^{-1} to 2000 cm^{-1}.

3. Results and Discussion

From EDX mapping, we deduce that the additions of Ge and Bi are not localized in the form of precipitates, but are present in the form of a solid solution in the Mg_2Si matrix. Figure S3 illustrates EDX elemental mapping carried out over a selected region (the pink box) within the grain with Ge (red) and Bi (green) colour coded maps. Atomic-level characterization work was carried out to confirm this as discussed later. The elemental maps corresponding to Ge (red) and Bi (green) indicate that the Ge and Bi atoms are alloyed with the Mg_2Si matrix in the form of solid solution. Low-magnification STEM imaging as shown in Figure 1a revealed the polycrystalline nature of the sample with larger grain sizes (< 12 μm). In addition, the grain-boundaries can be seen as brighter as compared to the bulk of the grain. The reason for the brighter intensities is consistent with the segregation of elements with higher *Z* (in this case, Ge and/or Bi). EDX mapping performed on the area highlighted as a rectangle, i.e. including three different grains and their grain boundaries, revealed a mostly homogenous presence of Mg, Si, and Bi within the grains, while Ge was accumulated along the grain boundaries, but with higher concentration in some of the grains (the top grain in the particular case shown in the map of Figure 1). To further analyze this, additional line scans were performed, as highlighted on the left of Figures 1b and 1c. Going from the left grain to the bottom grain (Figure 1b), the Ge concentration peaked in the boundary between these two. On the other hand, the line scan from the top to the bottom grain (Figure 1c) revealed a higher Ge concentration in the top grain, while Bi stayed constant within error of the method.

Figure 1 here

The low-magnification STEM-HAADF image shown in Figure 2a illustrates an area along the edge of the specimen. The Kikuchi diffraction patterns obtained on two different spots (Figures 2b and 2c) confirm the presence of two grains with different orientations and, hence, a grain boundary at the interface. In fact, the grain boundary is visible as a bright stripe midway between the spots where the Kikuchi patterns are obtained. EDX line scans were performed for Ge and Bi as shown in the Figure 2d and 2e to examine the distribution of heavy elements. From the line profile of Ge, it is evident that Ge is segregating along the grain boundary, consistent with the findings discussed above. Again in contrast to Ge, the EDX intensity in the line profile of Bi does not reveal any such segregation, but possibly slightly different concentrations in the

two grains. The apparent large width of the Ge segregation profile (Figure 2e) can be explained by the fact that, in this particular region and sample tilt, the grain boundary might not be perfectly parallel to the electron beam. The segregation of Ge at the grain boundaries together with the homogenous distribution of Bi in the grain boundaries could be helpful in blocking the phonons while allowing the electrons to pass. To obtain better statistics, other grain boundaries were analyzed (not shown), and were found to be consistent over all observed ones. Compared to our earlier work (Mg_2Si with Bi and no Ge), the Bi atoms were found to extensively segregate along the grain boundaries.[26,27] Here the segregation, if at all present, would be very small compared to the previously studied samples. This implies that it is possible to tune the segregation/distribution behaviors of dopants by increasing the unit cell through alloying.

Figure 2 here

In addition to EDX line scans as well as low-magnification imaging illustrated above, the distribution of dopants within a grain was understood better using STEM-HAADF imaging performed at an atomic resolution, as shown in Figure 3a. For better visibility, a selected region is magnified and shown in Figure 3b. Individual atomic columns of the doped Mg_2Si lattice, oriented along the [111] zone axis, are visible in Figure 3b. In these *Z*-contrast imaging conditions, the brighter atomic columns on the image (identified with pink arrows) are distributed randomly over the entire 2-D projection of the lattice, and contain heavier elements such as Ge and Bi, which are located on substitutional sites replacing Si atoms.[26,27] It is clear that the dopant atoms are rather homogenously distributed within the bulk of the grain. Figure 3c illustrates this in much better clarity where a site with significantly brighter intensity (pink arrow) can be clearly seen in proximity to another site with relatively weaker intensity (green arrow).

Figure 3 here

Raman spectra of $Mg_2Si_{0.877}Ge_{0.1}Bi_{0.023}$ with different amounts of MWCNT are shown in Figure 4. The pure MWCNT was also measured as the reference. As can be seen, all the samples demonstrate the higher frequency D mode (disordered) and G mode[28,29] at around 1350 $cm^{-1}$and

1590 cm^{-1}, respectively. No shift is observed in the D and G bands, which indicates the CNTs neither decomposed under pressure used for consolidation nor reacted with the base material. Although the regular breathing mode is specific to CNT, we cannot observe this mode for multi-wall carbon nanotube due to the larger strains of multi wall nanotubes, which hinder its vibration along the radial direction compared to the single wall carbon nanotubes.[30]

Figure 4 here

The electrical conductivity of all the nanocomposites is shown in Figure 5. For all samples, the electrical conductivity increases with temperature below 600 K and then decreases due to an increase in electron-phonon interaction, which dominates charge carrier scattering at higher temperature. Adding multi wall carbon nanotubes increases the electrical conductivity from $\sigma = 450\ \Omega^{-1}cm^{-1}$ for the sample without MWCNT to $500\ \Omega^{-1}cm^{-1}$ for the sample containing 0.5 weight-% MWCNT at 323 K.

Figure 5 here

The main reason for the increased electrical conductivity is due to the increase in n (Figure 6), since the mobility (μ_H) (Figure 7) of all the samples is very similar. The sample containing 0.5 wt.% MWCNT shows the highest carrier concentration on average below 300 K with the maximum value of around 8.4×10^{19} per cm^3 at 280 K. Although increasing the amount of carbon nanotubes slightly decreases the carrier concentration, the undoped sample exhibits the lowest on average. The mobility of all samples increases with temperatures, which could be due to the existence of MgO at the grain boundaries, which dominates the grain boundary scattering at lower temperature[27] as also observed in Sb-doped Mg_2Si.[31]

Figures 6 and 7 here

A comparison between different Bi-doped Mg_2Si nanocomposites is given in Table 1. The 0.5 wt.-% MWCNT sample shows an electrical conductivity of $\sigma = 470\ \Omega^{-1}cm^{-1}$ at 773 K, which is in between the SWCNH and the Si nanoparticle composite samples with $\sigma = 312\ \Omega^{-}$

$^{1}cm^{-1}$ and 658 $\Omega^{-1}cm^{-1}$, respectively. The main difference between the electrical conductivity of the MWCNT-containing sample and the one containing Si nanoparticles is due to the 50 percent higher carrier concentration of 11.7×10^{19} per cm^3 of the latter.

Table 1 here

Figure 8 exhibits the temperature dependence of the Seebeck coefficient. All the composites show a negative Seebeck value, indicative of electrons as the major charge carriers. The Seebeck value is around $S = -100$ μV K^{-1} at 323 K in every case, and it increases with increasing temperature. For the samples containing MWCNT, the increase is more noticeable, at 773 K with $S = -200$ μV K^{-1} for the 0.5 wt.-% MWCNT composite compared to $S = -180$ μV K^{-1} for the pristine sample. Thus, adding MWCNT resulted in an enhancement in Seebeck coefficient while maintaining the electrical conductivity. This phenomenon was also observed in $(Bi_{0.2}Sb_{0.8})_2Te_3$/MWCNT nanocomposites,[17] and can be attributed to the energy filtering of the low energy charge carriers,[32–35] which is a common phenomenon in nanocomposites due to the nanophase-matrix interface.[36] On the other hand, the SWCNH sample has a slightly higher (absolute) Seebeck coefficient ($S = -215$ μV K^{-1}), which is related to its noticeably low electrical conductivity (Table 1).

Figure 8 here

The capability of a thermoelectric material to generate electrical power is measured by the power factor, $P.F. = S^2\sigma$, which is demonstrated in Figure 9. The power factor of all samples starts around 5 μW $cm^{-1}K^{-2}$ at 323 K and increases with temperature. Except for the pristine sample, which reaches its maximum power factor of roughly 16 μW $cm^{-1}K^{-2}$ at around 673 K, all the nanocomposites show their highest value at around 773 K, with the 0.5 wt.-% MWCNT sample attaining ~ 19 μW $cm^{-1}K^{-2}$. Obtaining higher power factors would lead to higher output power density which makes the material more suitable for practical use.[37]

Figure 9 here

Figure 10 shows the thermal conductivity of all nanocomposites studied in this work, which was calculated based on the measured thermal diffusivity data. Because of the dominant acoustic phonon scattering, the thermal conductivity of all samples decreases with increasing temperature. The 1.5 wt.-% MWCNT sample demonstrates the lowest thermal conductivity of 2.07 W $m^{-1}K^{-1}$, which is substantially lower than that of the samples containing SWCNH and Si nanoparticle composites. This reduction in thermal conductivity can come from the combination of having both Ge and MWCNT in the sample. Since the thermal conductivity of MWCNT is increasing with temperature,[38] the propitious effect of MWCNT on thermal conductivity of nanocomposites is more dominant in the medium temperature range (Figure S4).

Figure 10 here

The electronic thermal conductivity, κ_e, was calculated by applying the Wiedemann-Franz law $\kappa_e = L\sigma T$. The Lorenz numbers, L, that were used in calculating κ_e are shown in Figure S5 and were obtained from Equation (1) by utilizing the single parabolic band and elastic carrier scattering estimation:

$$L = \left(\frac{k_B}{e}\right)^2 \left\{\frac{(1+\lambda)(3+\lambda)F_\lambda(\eta)F_{2+\lambda}(\eta) - (2+\lambda)^2 F_{1+\lambda}^2(\eta)}{(1+\lambda)^2 F_\lambda^2(\eta)}\right\} \quad (1)$$

where k_B and e are the Boltzmann constant and the electron charge, respectively. The Fermi integral of order j is depicted as $F_j(\eta)$, where η is the reduced Fermi energy (E_F) and is equal to $E_F/(k_B T)$. By assuming acoustic phonon scattering of the carriers ($\lambda = 0$),[39] The temperature dependence of η can be determined from the experimental Seebeck coefficient using Eq. (2):

$$S = \frac{k_B}{e}\left\{\frac{(2+\lambda)F_{1+\lambda}(\eta)}{(1+\lambda)F_\lambda(\eta)} - \eta\right\} \quad (2)$$

The electronic thermal conductivity of all samples is nearly the same and it increases approximately from 0.3 W $m^{-1}K^{-1}$ at 323 K to 0.6 W $m^{-1}K^{-1}$ at 773 K, which leads us to the conclusion that the reduction in thermal conductivity is chiefly coming from changes in the

lattice contribution (Figure 11). The sample containing 1.5 wt.-% MWCNT depicts the lowest lattice thermal conductivity of 1.49 W $m^{-1}K^{-1}$ at 773 K, compared to 2.85 W $m^{-1}K^{-1}$ and 2 W $m^{-1}K^{-1}$ determined for the SWCNH and Si nanoparticle composites, respectively.

Figure 11 here

After measuring all the thermoelectric properties, the thermoelectric figure of merit *zT* was computed (Figure 12). The *zT* of all composites increases with increasing temperature. While all the nanocomposites show higher *zT* than the pristine sample, the 0.5 wt.-% MWCNT sample reaches a maximum value of $zT = 0.67$ at 773 K among all MWCNT. This matches *zT* of the Si nanoparticle counterpart, and is more than twice of what was achieved for the Bi doped SWCNH composites.

Figure 12 here

One of the main issues in thermoelectric nanocomposites research is the homogeneity of the distributed nano phase in the matrix and its effect on the properties of the nanocomposites. To examine the reliability of the presented data, a second bar was cut from a different part of the 0.5 wt.-% MWCNT pellet, and the obtained power factor (Figure S6) is equal within experimental error.

4. Conclusions

Atomic resolution imaging and EDX analyses on $Mg_2Si_{0.877}Ge_{0.1}Bi_{0.023}$/0.5 wt.-% MWCNT sample revealed a rather homogenous distribution of Ge and Bi in the bulk of the grains, although Ge partially segregates along the grain boundaries. With *Z*-contrast imaging, we have shown the random distribution in solid solution of Bi and Ge atoms in the Mg_2Si lattice ultimately leading to local lattice distortions of the lattice due to size effects. The inclusion of multi-wall carbon nanotubes into $Mg_2Si_{0.877}Ge_{0.1}Bi_{0.023}$ matrix at low concentration not only maintained the high temperature electrical conductivity, but also led to a 10% improvement of the high temperature Seebeck coefficient, which could be due to energy filtering that originated from the $Mg_2Si_{0.877}Ge_{0.1}Bi_{0.023}$ - MWCNT matrix interfaces.

Although the existence of MWCNT enhanced phonon scattering especially at medium temperature lowered the lattice thermal conductivity, this reduction is compensated at higher temperature due to the thermal transport behavior of MWCNT. The positive effect of MWCNT on thermoelectric properties of $Mg_2Si_{0.877}Ge_{0.1}Bi_{0.023}$ is manifested by the enhanced thermoelectric figure of merit, *zT*, with all the nanocomposites achieving higher *zT* values than the pristine sample. The highest improvement of more than 20% belongs to the sample containing 0.5 wt.-% MWCNT with its *zT* of 0.67 at 773 K. Comparing with the other nano inclusions that were applied to Mg_2Si based thermoelectrics, MWCNT exhibited the most promising effect on TE properties, and further development may be implemented through adding tin or in situ nano-structuring via ball milling.

Acknowledgment

The authors would like to thank AUTO21 (Network Centres of Excellence) and General Motors for financial support of this work. The STEM and EDX work was performed at the Canadian Centre for Electron Microscopy, a national facility supported by NSERC, the Canada Foundation for Innovation and McMaster University.

Supplementary Information

X-ray powder diagrams of $Mg_2Si_{0.877}Ge_{0.1}Bi_{0.023}$/x wt.-% MWCNT ($0 \leq x \leq 1.5$). SEM images of MWCNT within the $Mg_2Si_{0.877}Ge_{0.1}Bi_{0.023}$ matrix. Low-magnification STEM-HAADF images of grain and grain boundaries together with elemental mapping. Medium temperature thermal conductivity with regard to MWCNT content. Temperature dependency of calculated Lorenz number. Power factor comparison of two bars obtained from the same nanocomposite. Density and specific heat of all the composites.

References

1 S. Iijima, *Nature*, 1991, **354**, 56–58.

2 K. Balasubramanian and M. Burghard, *Small*, 2005, **1**, 180–192.

3 F. Yang, X. Wang, D. Zhang, J. Yang, D. Luo, Z. Xu, J. Wei, J.-Q. Wang, Z. Xu, F. Peng, X. Li, R. Li, Y. Li, M. Li, X. Bai, F. Ding and Y. Li, *Nature*, 2014, **510**, 522–524.

4 K. M. Choi, S. Augustine, J. H. Choi, J. H. Lee, W. H. Shin, S. H. Yang, J. Y. Lee and J. K. Kang, *Angew. Chem. Int. Ed. Engl.*, 2008, **47**, 9904–9907.

5 M. V. Vedernikov and E. K. Iordanishvili, in *Seventeenth International Conference on Thermoelectrics. Proceedings ICT98*, IEEE, 1998, pp. 37–42.

6 T. M. Tritt, *Annu. Rev. Mater. Res.*, 2011, **41**, 433–448.

7 H. Kleinke, *Chem. Mater.*, 2010, **22**, 604–611.

8 S. V Faleev and F. Léonard, *Phys. Rev. B*, 2008, **77**, 214304/1–214304/9.

9 M. Zebarjadi, K. Esfarjani, A. Shakouri, J.-H. Bahk, Z. Bian, G. Zeng, J. Bowers, H. Lu, J. Zide and A. Gossard, *Appl. Phys. Lett.*, 2009, **94**, 202105.

10 M. S. Dresselhaus, G. Chen, M. Y. Tang, R. G. Yang, H. Lee, D. Z. Wang, Z. F. Ren, J.-P. Fleurial and P. Gogna, *Adv. Mater.*, 2007, **19**, 1043–1053.

11 T. Ando, *NPG Asia Mater.*, 2009, **1**, 17–21.

12 C. Qin, X. Shi, S. Q. Bai, L. D. Chen and L. J. Wang, *Mater. Sci. Eng. A*, 2006, **420**, 208–211.

13 D. Suh, D. Lee, C. Kang, I.-J. Shon, W. Kim and S. Baik, *J. Mater. Chem.*, 2012, **22**, 21376–21381.

14 F. Ren, H. Wang, P. A. Menchhofer and J. O. Kiggans, *Appl. Phys. Lett.*, 2013, **103**, 221907.

15 Y. Zhang, X. L. Wang, W. K. Yeoh, R. K. Zheng and C. Zhang, *Appl. Phys. Lett.*, 2012, **101**, 031909.

16 K. T. Kim, S. Y. Choi, E. H. Shin, K. S. Moon, H. Y. Koo, G.-G. Lee and G. H. Ha, *Carbon N. Y.*, 2013, **52**, 541–549.

17 Y. H. Yeo and T. S. Oh, *Mater. Res. Bull.*, 2014, **58**, 54–58.

18 J. Yang and F. R. Stabler, *J. Electron. Mater.*, 2009, **38**, 1245–1251.

19 S. Fiameni, S. Battiston, S. Boldrini, A. Famengo, F. Agresti, S. Barison and M. Fabrizio, *J. Solid State Chem.*, 2012, **193**, 142–146.

20 D. Cederkrantz, N. Farahi, K. A. Borup, B. B. Iversen, M. Nygren and A. E. C. Palmqvist, *J. Appl. Phys.*, 2012, **111**, 023701.

21 T. Yi, S. Chen, S. Li, H. Yang, S. Bux, Z. Bian, N. a. Katcho, A. Shakouri, N. Mingo, J.-P. Fleurial, N. D. Browning and S. M. Kauzlarich, *J. Mater. Chem.*, 2012, **22**, 24805.

22 V. K. Zaitsev, M. I. Fedorov, E. A. Gurieva, I. S. Eremin, P. P. Konstantinov, A. Y. Samunin and M. V Vedernikov, *Phys. Rev. B*, 2006, **74**, 045207/1–045207/5.

23 R. J. LaBotz, D. R. Mason and D. F. O'Kane, *J. Electrochem. Soc.*, 1963, **110**, 127–134.

24 E. Ratai, M. P. Augustine and S. M. Kauzlarich, *J. Phys. Chem. B*, 2003, **107**, 12573–12577.

25 T. Ikeda, L. Haviez, Y. Li and G. J. Snyder, *Small*, 2012, **8**, 2350–2355.

26 N. Farahi, S. Prabhudev, G. Botton, J. Zhao, J. S. Tse, Z. Liu, J. R. Salvador and H. Kleinke, *J. Alloy. Compd.*, 2015, **644**, 249–255.

27 N. Farahi, M. VanZant, J. Zhao, J. S. Tse, S. Prabhudev, G. Botton, J. R. Salvador, F. Borondics, Z. Liu and H. Kleinke, *Dalt. Trans.*, 2014, **43**, 14983–14991.

28 M. S. Dresselhaus, G. Dresselhaus, P. C. Eklund and A. M. Rao, in *The Physics of Fullerene-Based and Fullerene-Related Materials SE - 9*, ed. W. Andreoni, Springer Netherlands, 2000, vol. 23, pp. 331–379.

29 A. M. Rao, A. Jorio, M. A. Pimenta, M. S. S. Dantas, R. Saito, G. Dresselhaus and M. S. Dresselhaus, *Phys. Rev. Lett.*, 2000, **84**, 1820–1823.

30 J. H. Lehman, M. Terrones, E. Mansfield, K. E. Hurst and V. Meunier, *Carbon N. Y.*, 2011, **49**, 2581–2602.

31 J. de Boor, T. Dasgupta, H. Kolb, C. Compere, K. Kelm and E. Mueller, *Acta Mater.*, 2014, **77**, 68–75.

32 Y. Zhang, J.-H. Bahk, J. Lee, C. S. Birkel, M. L. Snedaker, D. Liu, H. Zeng, M. Moskovits, A. Shakouri and G. D. Stucky, *Adv. Mater.*, 2014, **26**, 2755–2761.

33 A. Shakouri, *Annu. Rev. Mater. Sci.*, 2011, **41**, 399–431.

34 A. Soni, Y. Shen, M. Yin, Y. Zhao, L. Yu, X. Hu, Z. Dong, K. A. Khor, M. S. Dresselhaus and Q. Xiong, *Nano Lett.*, 2012, **12**, 4305–4310.

35 N. D. Y. Truong, H. Kleinke and F. Gascoin, *Dalt. Trans.*, 2014, **43**, 15092–15097.

36 D. L. Medlin and G. J. Snyder, *Curr. Opin. Colloid Interface Sci.*, 2009, **14**, 226–235.

37 W. Liu, H. S. Kim, S. Chen, Q. Jie, B. Lv, M. Yao, Z. Ren, C. P. Opeil, S. Wilson, C.-W. Chu and Z. Ren, *Proc. Natl. Acad. Sci. U. S. A.*, 2015, **112**, 3269–3274.

38 R. Prasher, *Phys. Rev. B*, 2008, **77**, 075424.

39 V. I. Fistul', *Heavily Doped Semiconductors*, Springer New York, Boston, MA, 1995.

Figure captions

Fig. 1 (a) Left: low-magnification STEM-HAADF image; right: EDX elemental maps of Mg, Si, Ge and Bi in the area marked with a rectangle; (b), (c) line profiles of Ge-K and Bi-L lines along the boundary between different grains. The profiles in red and green correspond to Ge and Bi, respectively.

Fig. 2 (a) Low-magnification STEM-HAADF image; (b) and (c) Kikuchi patterns confirming two different grains separated by a grain boundary; (d) EDX line scans of Ge-K (red) and Bi-L (green) lines along the grain boundary; (e) line profiles of Ge (red) and Bi (green) along the grain boundary as shown in (d).

Fig. 3 (a) and (b) Atomic resolution STEM-HAADF images corresponding to a region in the bulk of a grain oriented along [111] zone axis; (c) magnified region from (b), the green arrow indicating an atomic column with no significant brighter intensities as compared to the atomic column highlighted by the pink arrow.

Fig. 4 Raman spectra of the $Mg_2Si_{0.877}Ge_{0.1}Bi_{0.023}$/MWCNT samples.

Fig. 5 Electrical conductivity of the $Mg_2Si_{0.877}Ge_{0.1}Bi_{0.023}$/MWCNT samples.

Fig. 6 Room temperature carrier concentration of the $Mg_2Si_{0.877}Ge_{0.1}Bi_{0.023}$/MWCNT samples.

Fig. 7 Low temperature Hall mobility of the $Mg_2Si_{0.877}Ge_{0.1}Bi_{0.023}$/MWCNT samples.

Fig. 8 Seebeck coefficient of the $Mg_2Si_{0.877}Ge_{0.1}Bi_{0.023}$/MWCNT samples.

Fig. 9 Power factor of MWCNT/$Mg_2Si_{0.877}Ge_{0.1}Bi_{0.023}$ samples.

Fig. 10 Thermal conductivity of the $Mg_2Si_{0.877}Ge_{0.1}Bi_{0.023}$/MWCNT samples.

Fig. 11 Lattice thermal conductivity of the $Mg_2Si_{0.877}Ge_{0.1}Bi_{0.023}$/MWCNT samples.

Fig. 12 Figure of merit of the $Mg_2Si_{0.877}Ge_{0.1}Bi_{0.023}$/MWCNT samples.

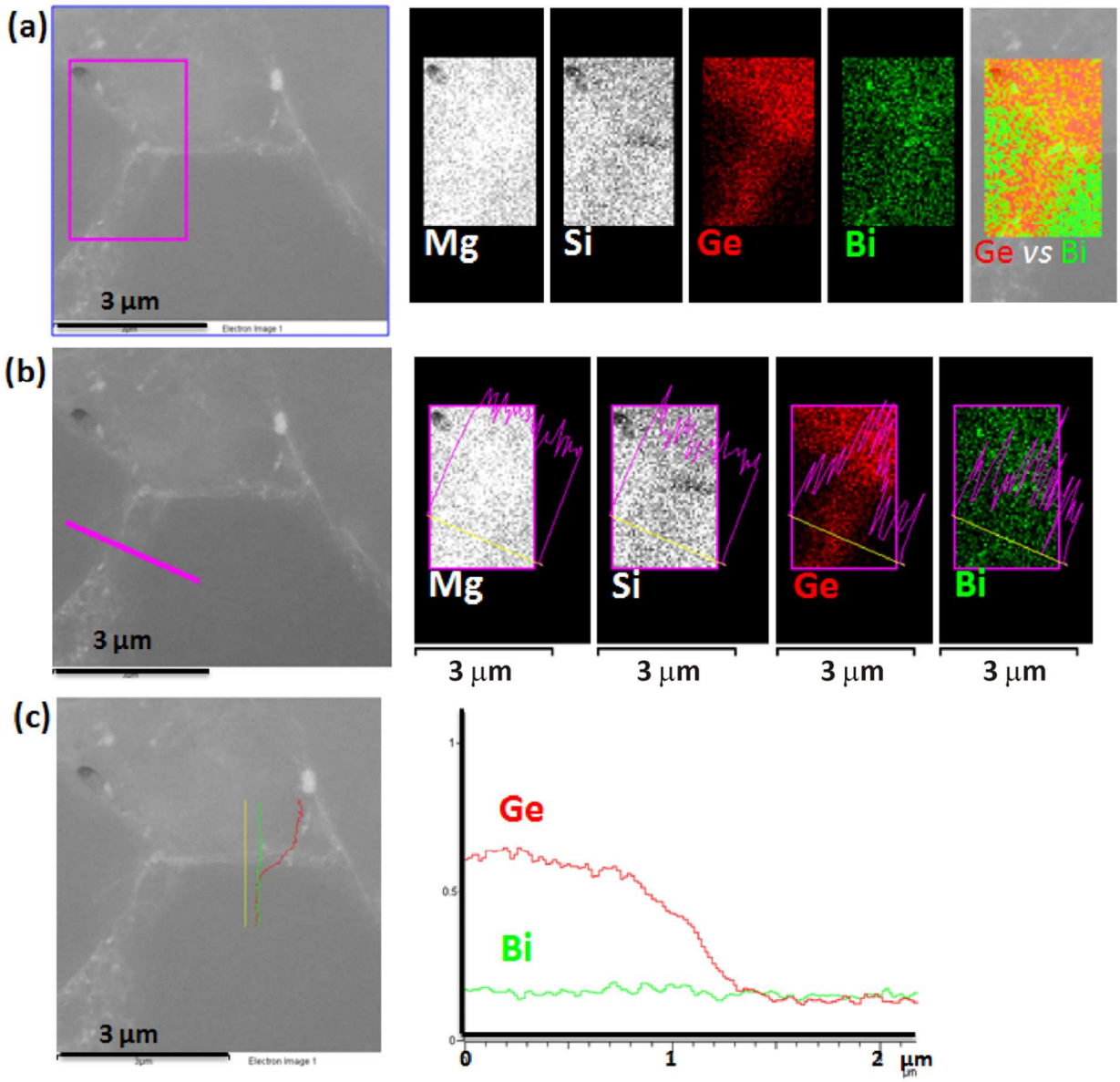

Fig. 1 (a) Left: low-magnification STEM-HAADF image; right: EDX elemental maps of Mg, Si, Ge and Bi in the area marked with a rectangle; (b), (c) line profiles of Ge-K and Bi-L lines along the boundary between different grains. The profiles in red and green correspond to Ge and Bi, respectively.

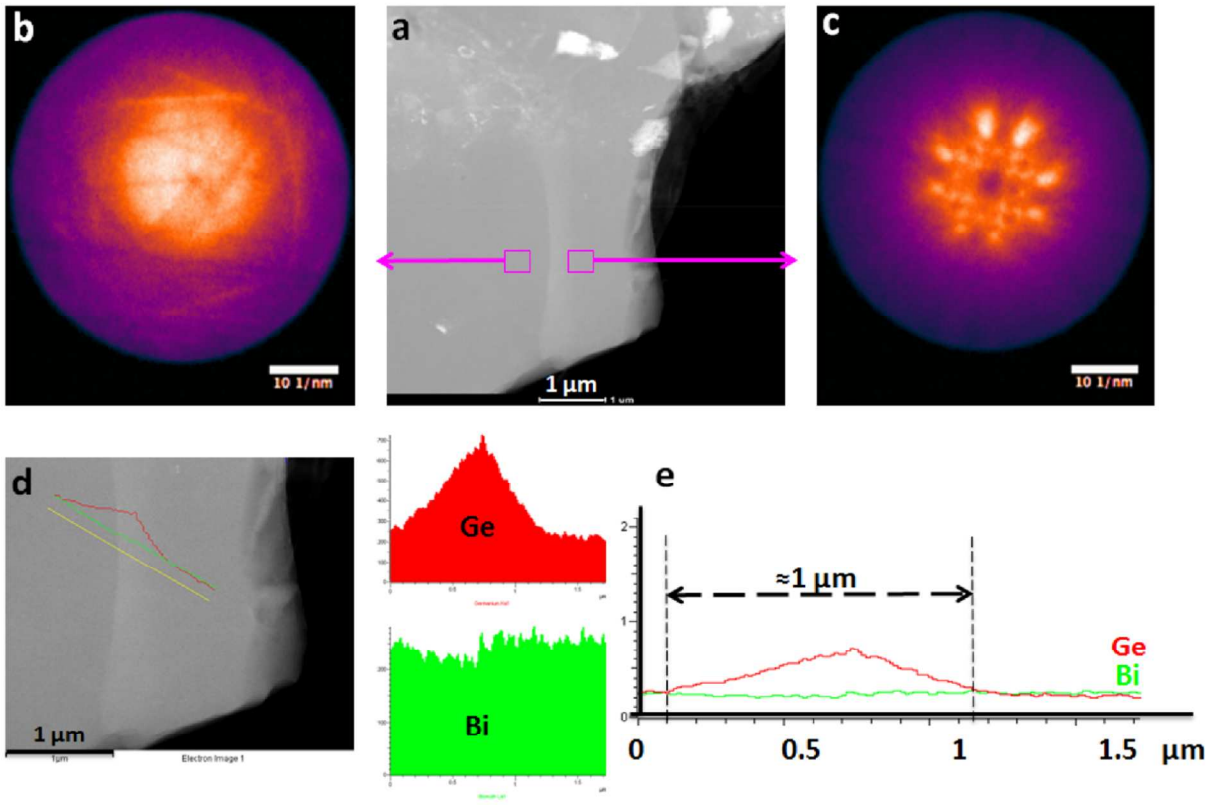

Fig. 2 (a) Low-magnification STEM-HAADF image; (b) and (c) Kikuchi patterns confirming two different grains separated by a grain boundary; (d) EDX line scans of Ge-K (red) and Bi-L (green) lines along the grain boundary; (e) line profiles of Ge (red) and Bi (green) along the grain boundary as shown in (d).

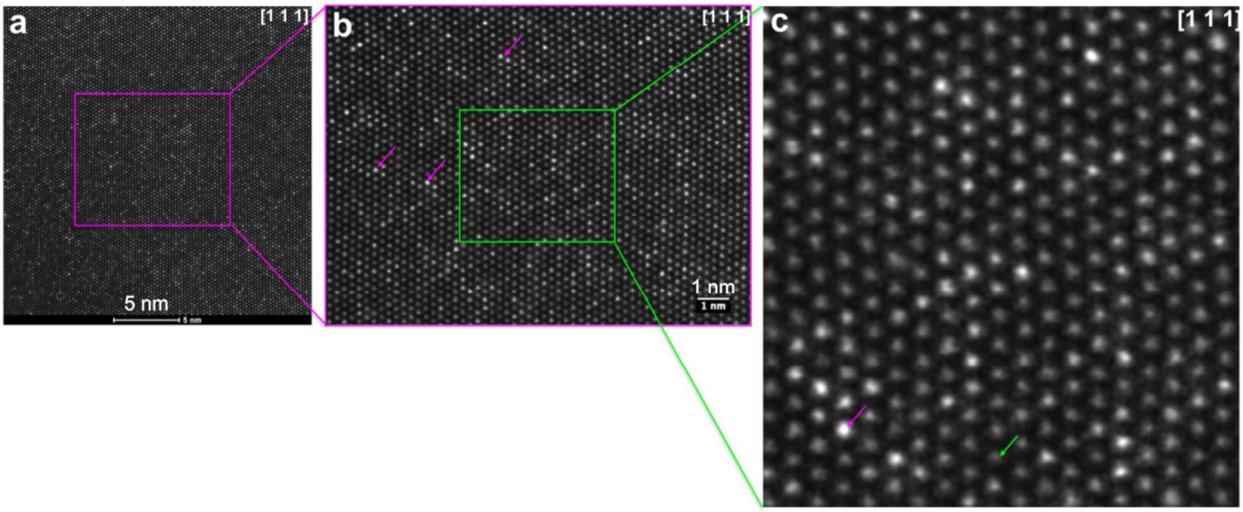

Fig. 3 (a) and (b) Atomic resolution STEM-HAADF images corresponding to a region in the bulk of a grain oriented along [111] zone axis; (c) magnified region from (b), the green arrow indicating an atomic column with no significant brighter intensities as compared to the atomic column highlighted by the pink arrow.

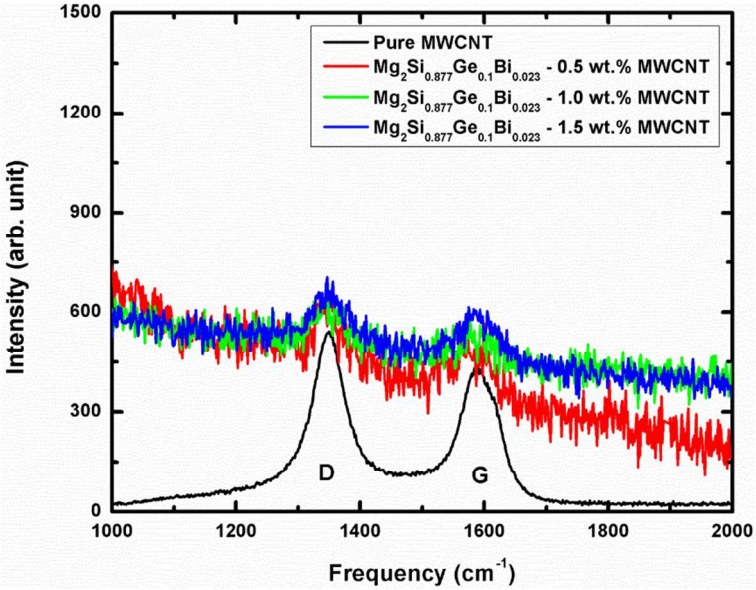

Fig. 4 Raman spectra of the $Mg_2Si_{0.877}Ge_{0.1}Bi_{0.023}$/MWCNT samples.

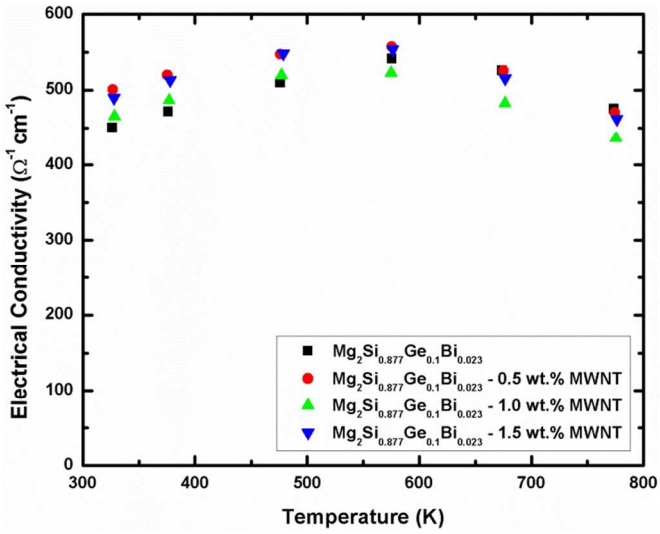

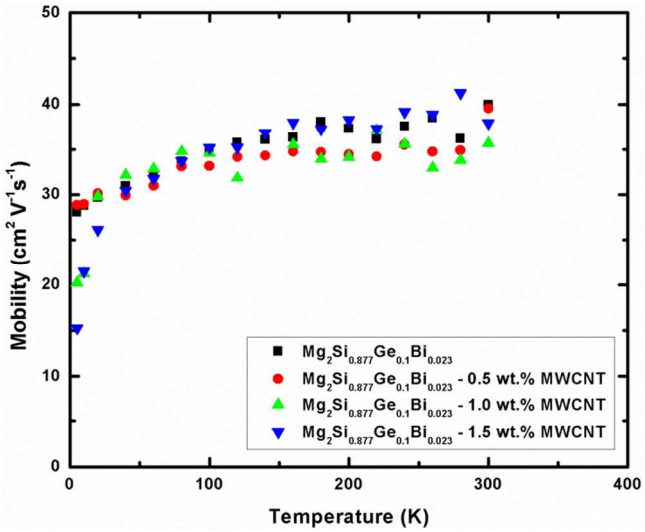

Fig. 5 Electrical conductivity of the $Mg_2Si_{0.877}Ge_{0.1}Bi_{0.023}$/MWCNT samples.

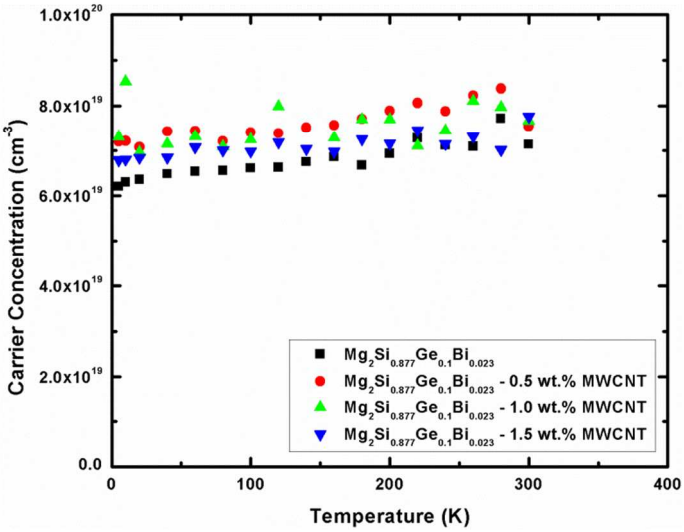

Fig. 6 Room temperature carrier concentration of the $Mg_2Si_{0.877}Ge_{0.1}Bi_{0.023}$/MWCNT samples.

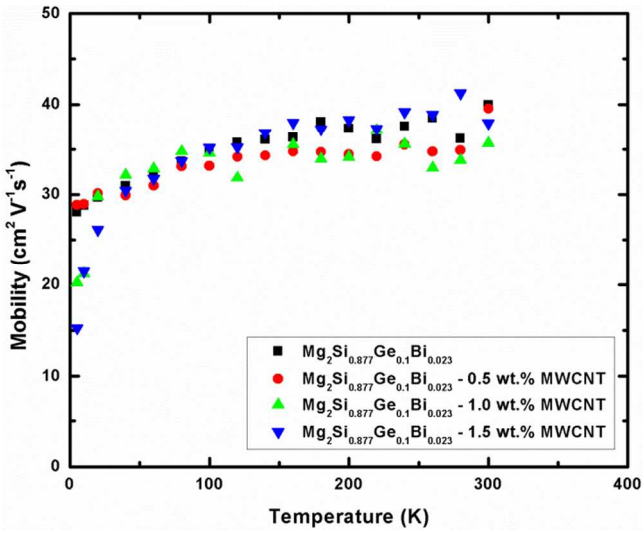

Fig. 7 Low temperature Hall mobility of the $Mg_2Si_{0.877}Ge_{0.1}Bi_{0.023}$/MWCNT samples.

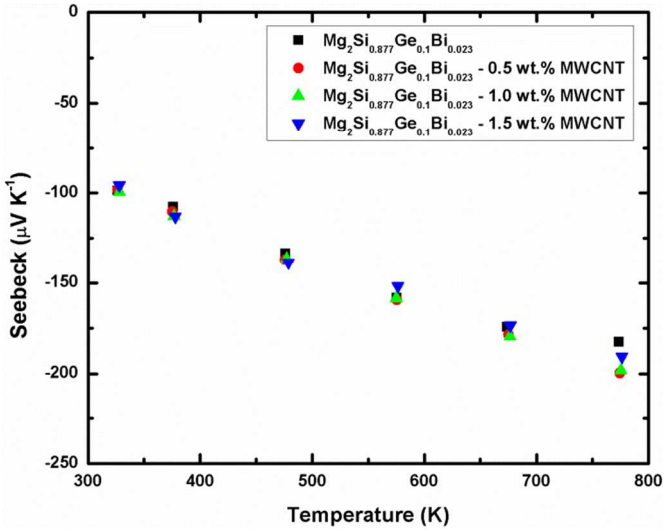

Fig. 8 Seebeck coefficient of the $Mg_2Si_{0.877}Ge_{0.1}Bi_{0.023}$/MWCNT samples.

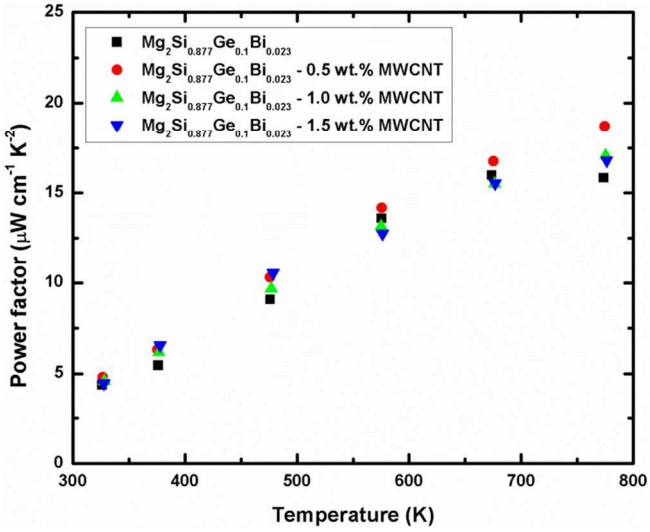

Fig. 9 Power factor of MWCNT/$Mg_2Si_{0.877}Ge_{0.1}Bi_{0.023}$ samples.

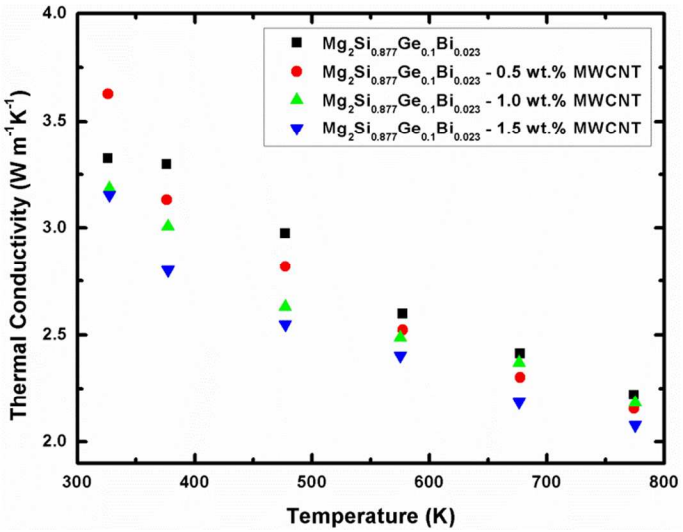

Fig. 10 Thermal conductivity of the $Mg_2Si_{0.877}Ge_{0.1}Bi_{0.023}$/MWCNT samples.

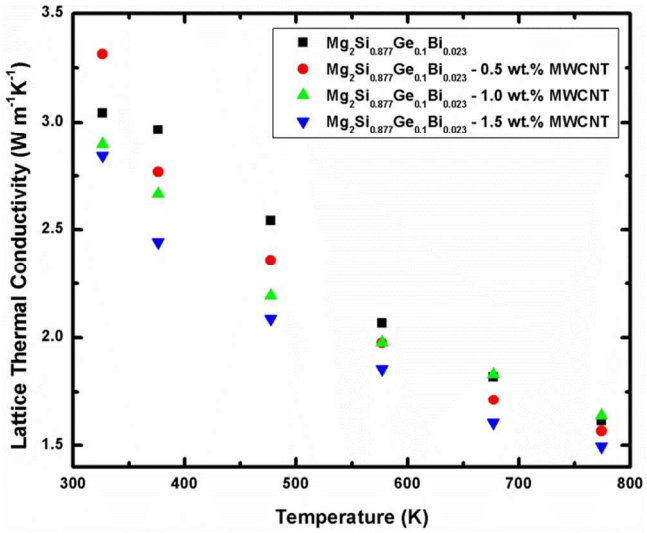

Fig. 11 Lattice thermal conductivity of the $Mg_2Si_{0.877}Ge_{0.1}Bi_{0.023}$/MWCNT samples.

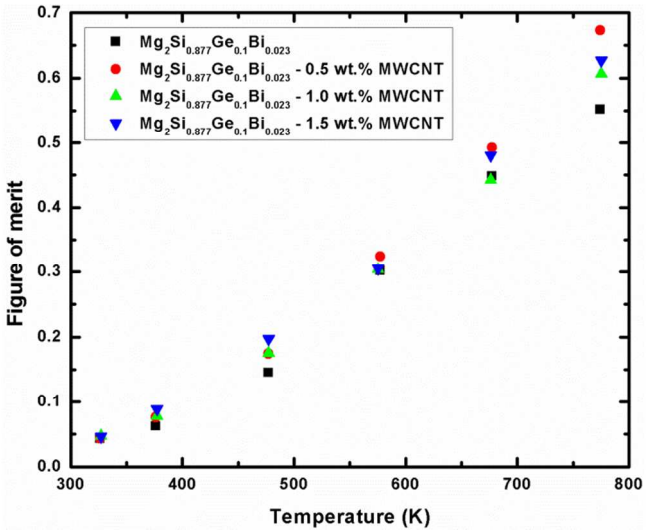

Fig. 12 Figure of merit of the $Mg_2Si_{0.877}Ge_{0.1}Bi_{0.023}$/MWCNT samples.

Table 1 Thermoelectric properties of $Mg_2Si_{0.877}Ge_{0.1}Bi_{0.023}$/0.5% MWCNT at 773 K in comparison to other Mg_2Si-based nanocomposites.

	$Mg_2Si_{0.877}Ge_{0.1}Bi_{0.023}$ / 0.5% MWCNT	Mg_2Si:$Bi_{0.02}$ / SWCNH [19]	Mg_2Si / 2.5 mol% $Si_{1\%Bi}$ [21]
$\sigma/(\Omega^{-1}cm^{-1})$	470	312	658
$S/(\mu V\ K^{-1})$	–200	–216	–204
$\kappa/(W\ m^{-1}K^{-1})$	2.2	3.4	3.1
$L/(10^{-8}\ V^2K^{-2})$	1.6	2.5	2.2
$\kappa_L/(W\ m^{-1}K^{-1})$	1.6	2.9	2.0
$\mu/(cm^2V^{-1}s^{-1})$ [300 K]	40	n/a	13
$n/(10^{19}\ cm^{-3})$ [300 K]	7.6	n/a	11.7
zT	0.67	0.32	0.67

Supplementary information

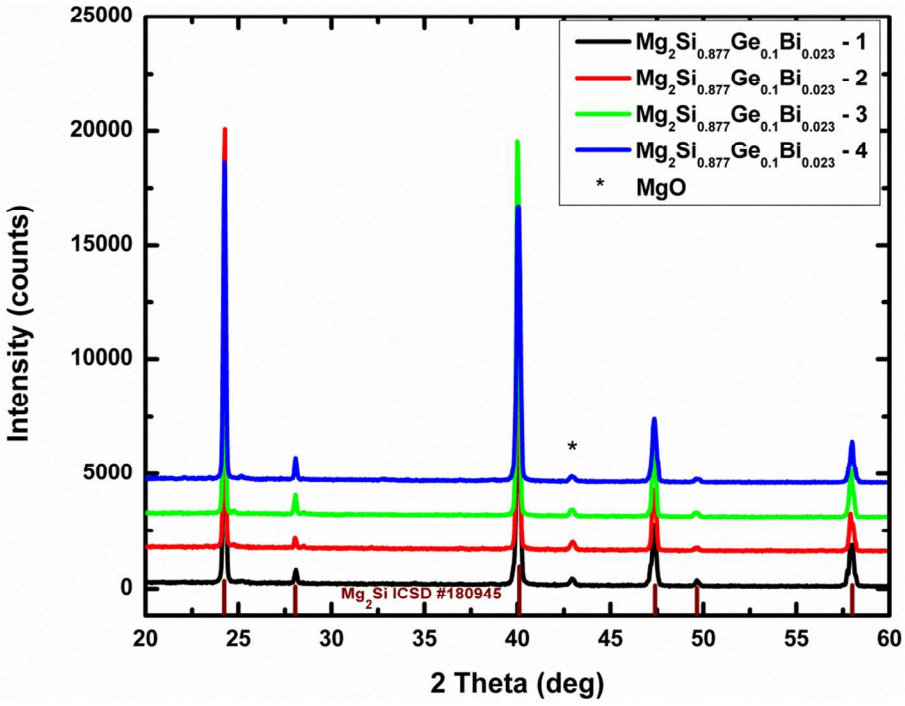

Fig. S1 Powder XRD patterns of $Mg_2Si_{0.877}Ge_{0.1}Bi_{0.023}$ samples.

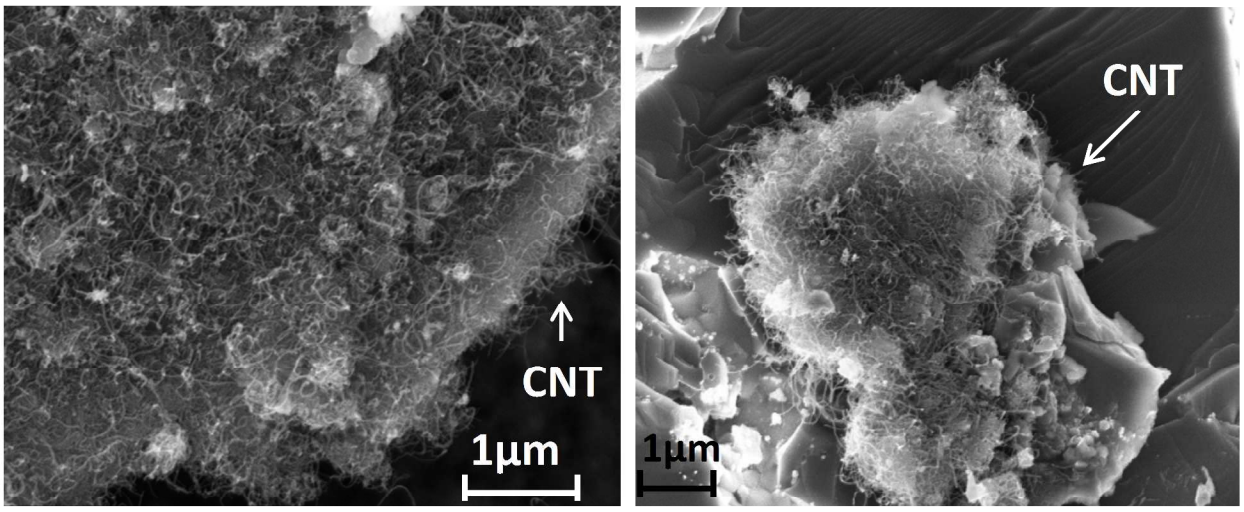

Fig. S2 SEM images of the $Mg_2Si_{0.877}Ge_{0.1}Bi_{0.023}$/1 wt.-% MWCNT sample.

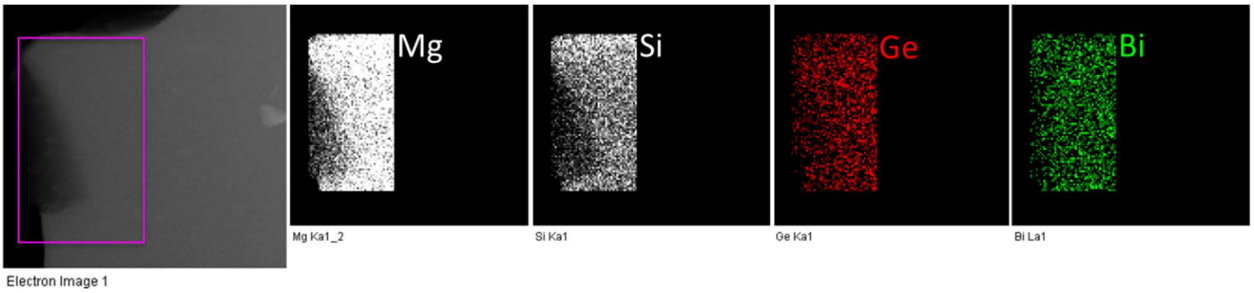

Fig. S3 Low-magnification structural (STEM-HAADF imaging) and compositional (EDX elemental mapping) analyses of a selected region within a grain. EDX elemental mapping shows the distribution of Mg, Si, Ge and Bi.

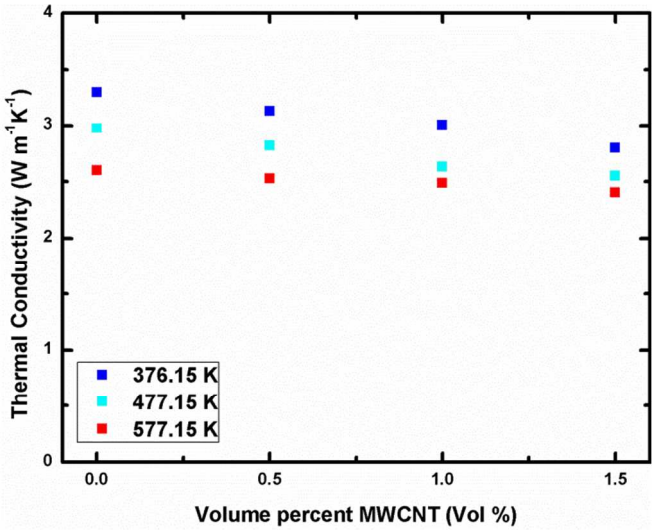

Fig. S4 Medium temperature thermal conductivity of all samples with respect to MWCNT content.

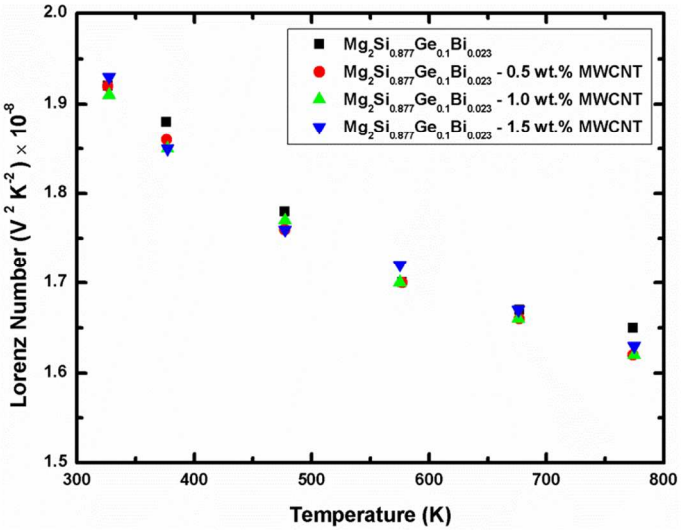

Fig. S5 Lorenz number of all samples with regard to temperature.

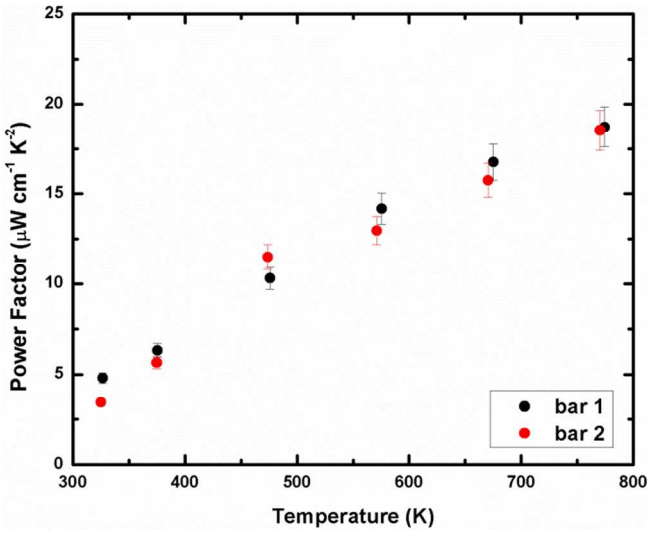

Fig. S6 Power factor of two bars obtained from 0.5% MWCNT/$Mg_2Si_{0.877}Ge_{0.1}Bi_{0.023}$ nanocomposite (6% error is considered).

Table S1 Densities and specific heat of the $Mg_2Si_{0.877}Ge_{0.1}Bi_{0.023}$/MWCNT samples.

Sample	Density ($g\ cm^{-3}$)	Relative density	C_p ($J\ g^{-1}K^{-1}$)
$Mg_2Si_{0.877}Ge_{0.1}Bi_{0.023}$	2.10	96%	0.877
$Mg_2Si_{0.877}Ge_{0.1}Bi_{0.023}$ - 0.5 wt.-% MWCNT	2.10	96%	0.882
$Mg_2Si_{0.877}Ge_{0.1}Bi_{0.023}$ - 1.0 wt.-% MWCNT	2.04	93%	0.888
$Mg_2Si_{0.877}Ge_{0.1}Bi_{0.023}$ - 1.5 wt.-% MWCNT	2.06	94%	0.894

Theoretical densities of the composite (d_C) were calculated using the mixture rule :

$$\frac{1}{d_C} = \frac{w_{MWCNT}}{d_{MWCNT}} + \frac{w_{Matrix}}{d_{Matrix}}$$

Where d_{MWCNT}, d_{Matrix}, W_{MWCNT} and W_{Matrix} are the densities and mass fractions of the nanotubes and $Mg_2Si_{0.877}Ge_{0.1}Bi_{0.023}$, respectively.

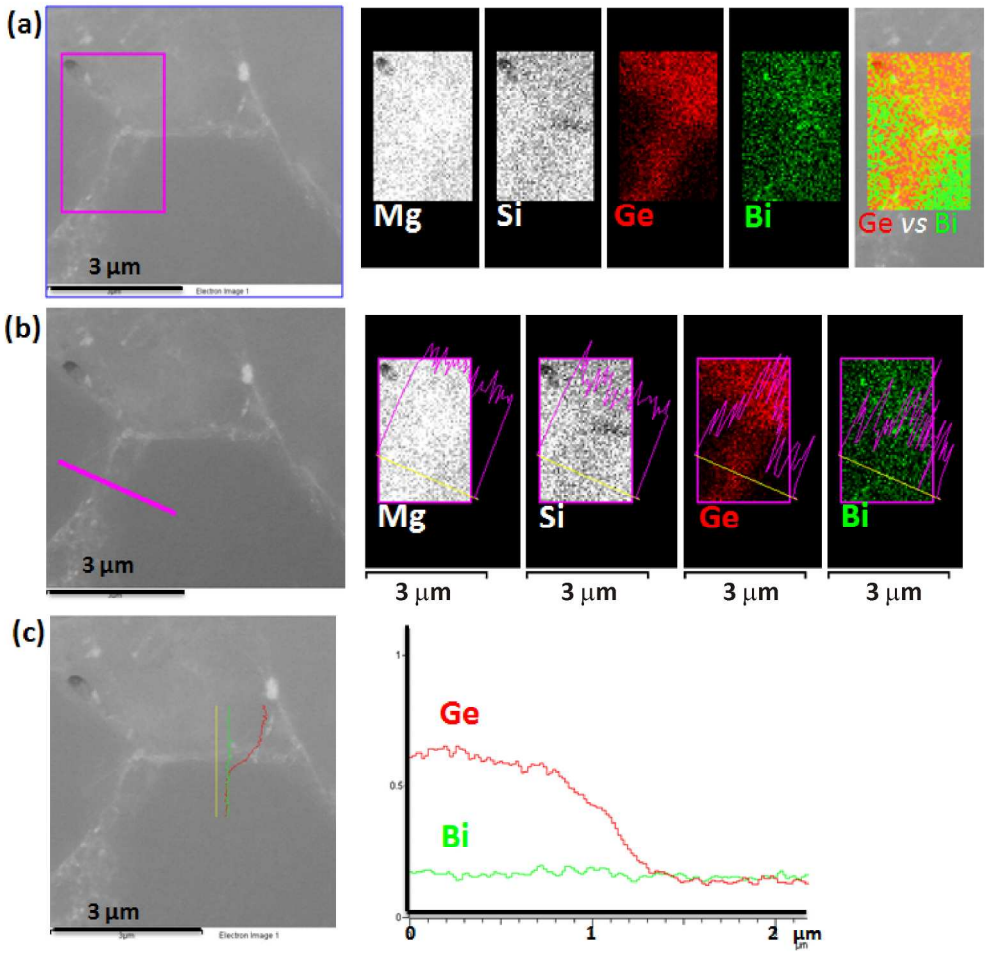

Fig. 1 (a) Left: low-magnification STEM-HAADF image; right: EDX elemental maps of Mg, Si, Ge and Bi in the area marked with a rectangle; (b), (c) line profiles of Ge-K and Bi-L lines along the boundary between different grains. The profiles in red and green correspond to Ge and Bi, respectively.
199x191mm (300 x 300 DPI)

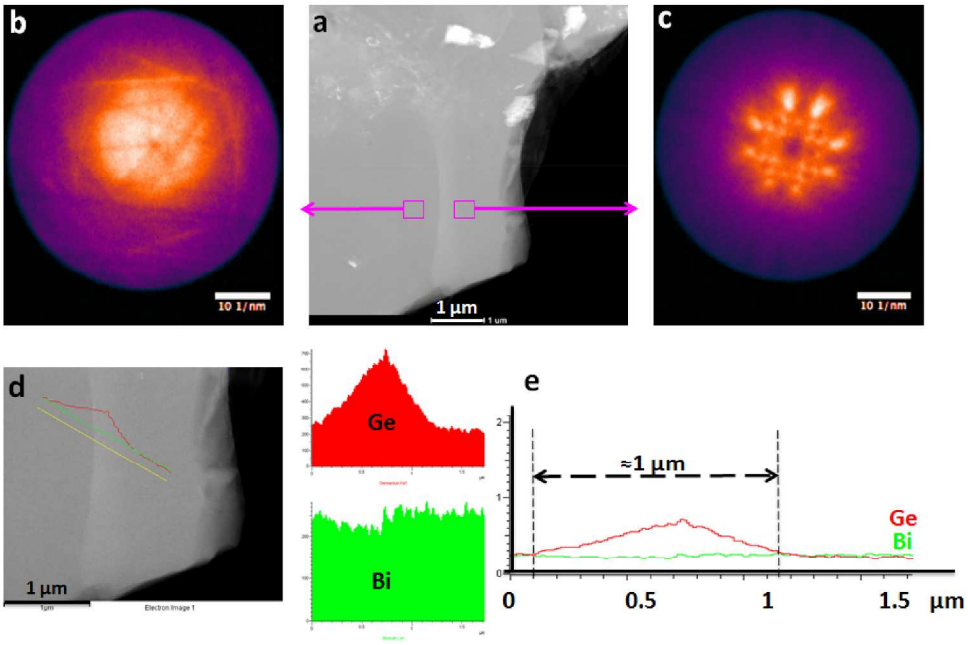

Fig. 2 (a) Low-magnification STEM-HAADF image; (b) and (c) Kikuchi patterns confirming two different grains separated by a grain boundary; (d) EDX line scans of Ge-K (red) and Bi-L (green) lines along the grain boundary; (e) line profiles of Ge (red) and Bi (green) along the grain boundary as shown in (d).
199x133mm (300 x 300 DPI)

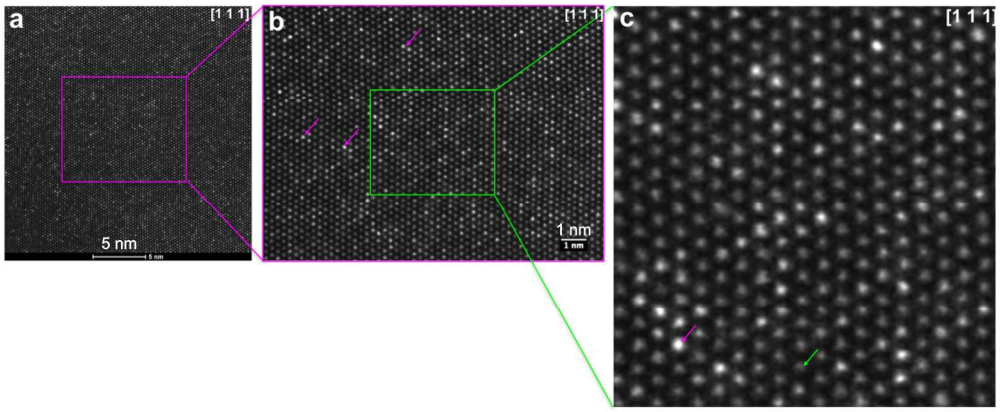

Fig. 3 (a) and (b) Atomic resolution STEM-HAADF images corresponding to a region in the bulk of a grain oriented along [111] zone axis; (c) magnified region from (b), the green arrow indicating an atomic column with no significant brighter intensities as compared to the atomic column highlighted by the pink arrow.
199x83mm (300 x 300 DPI)

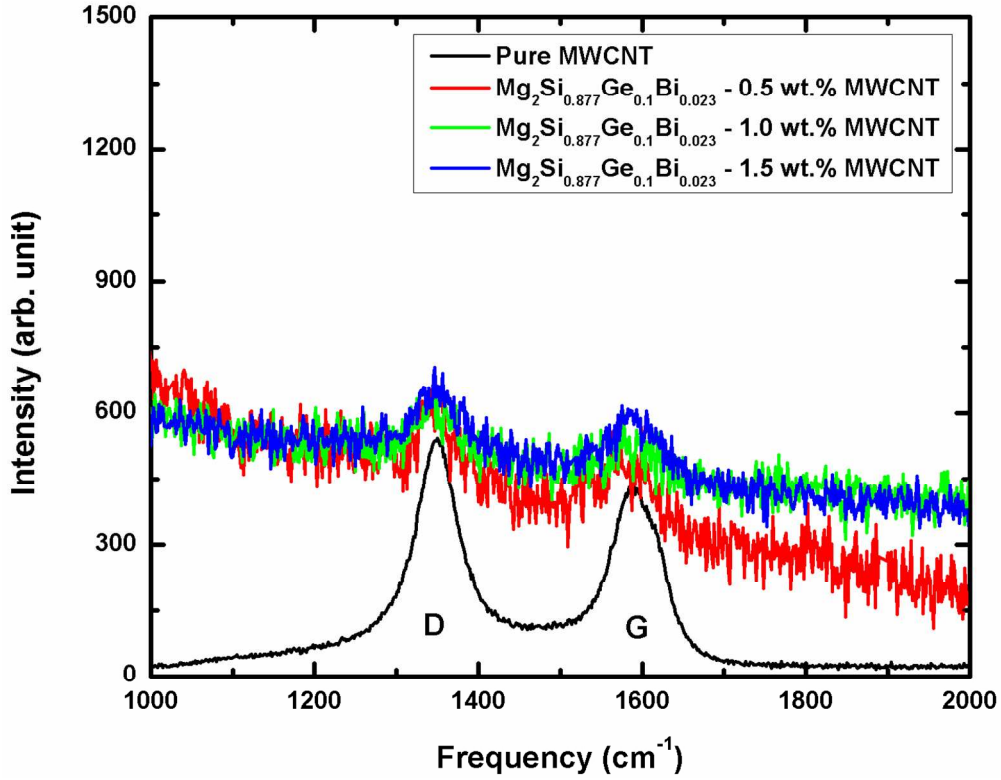

Fig. 4 Raman spectra of the Mg2Si0.877Ge0.1Bi0.023/MWCNT samples.
127x99mm (300 x 300 DPI)

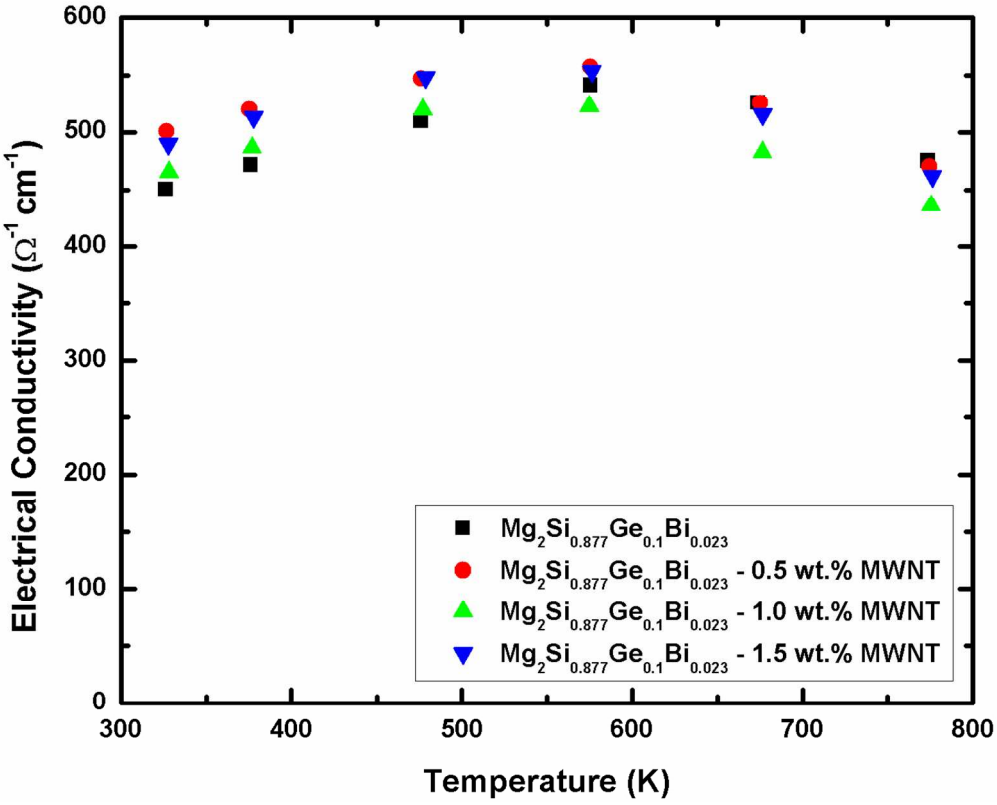

Fig. 5 Electrical conductivity of the Mg2Si0.877Ge0.1Bi0.023/MWCNT samples.
124x99mm (300 x 300 DPI)

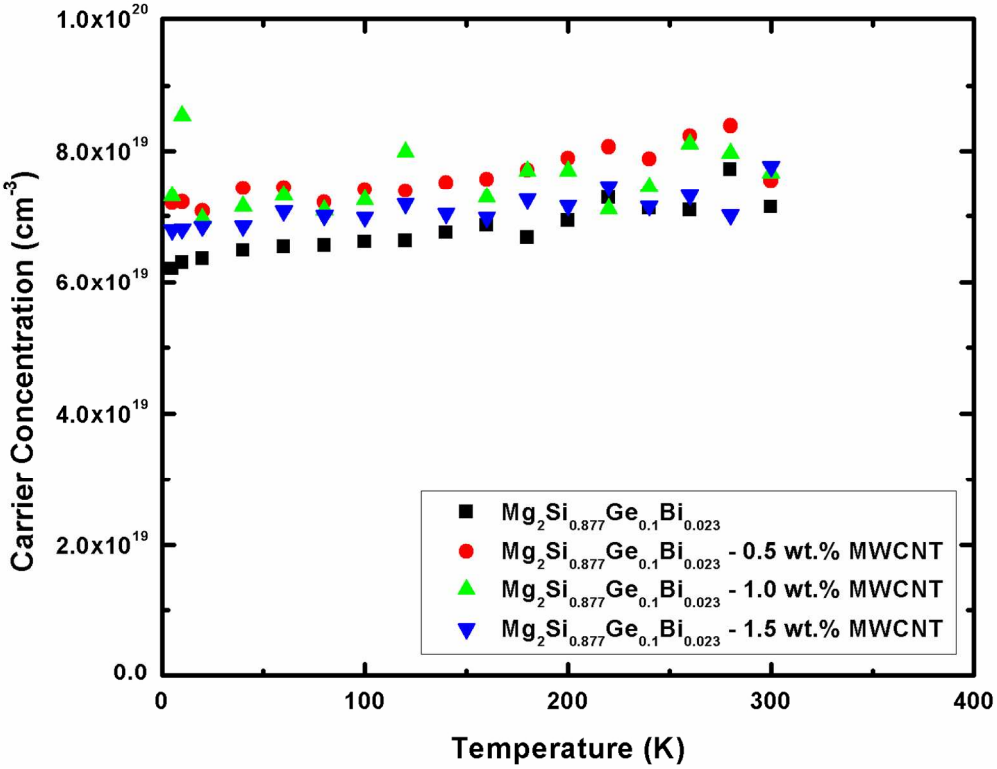

Fig. 6 Room temperature carrier concentration of the Mg2Si0.877Ge0.1Bi0.023/MWCNT samples.
129x99mm (300 x 300 DPI)

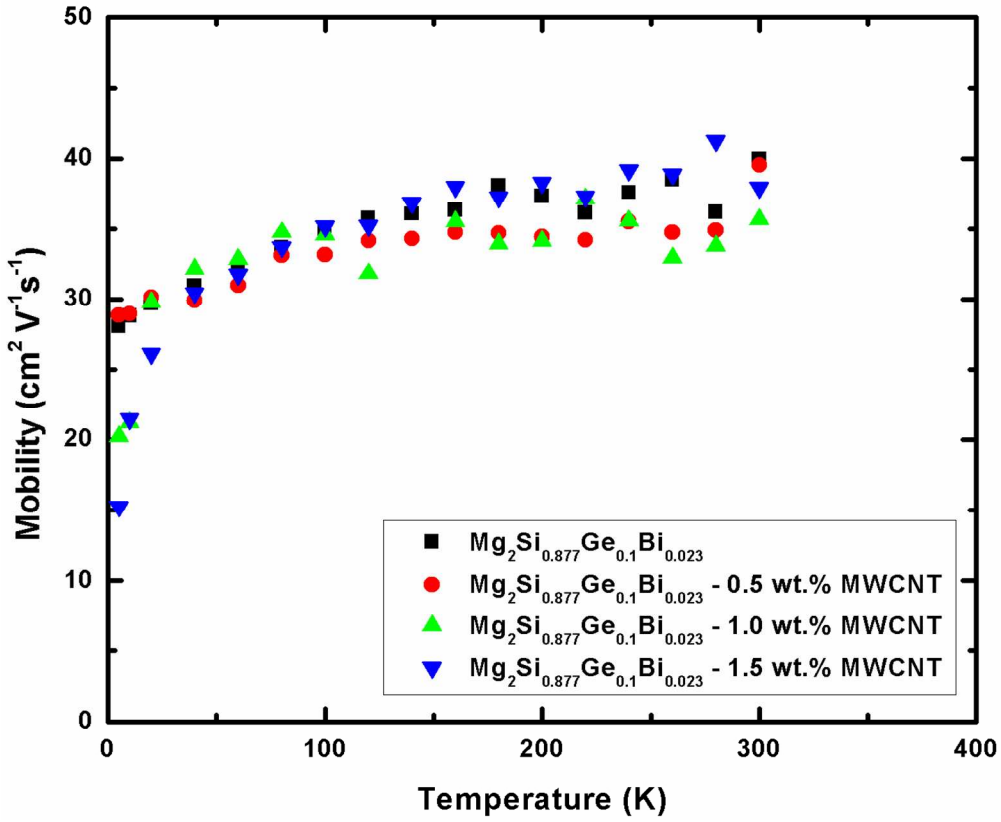

Fig. 7 Low temperature Hall mobility of the Mg2Si0.877Ge0.1Bi0.023/MWCNT samples.
121x99mm (300 x 300 DPI)

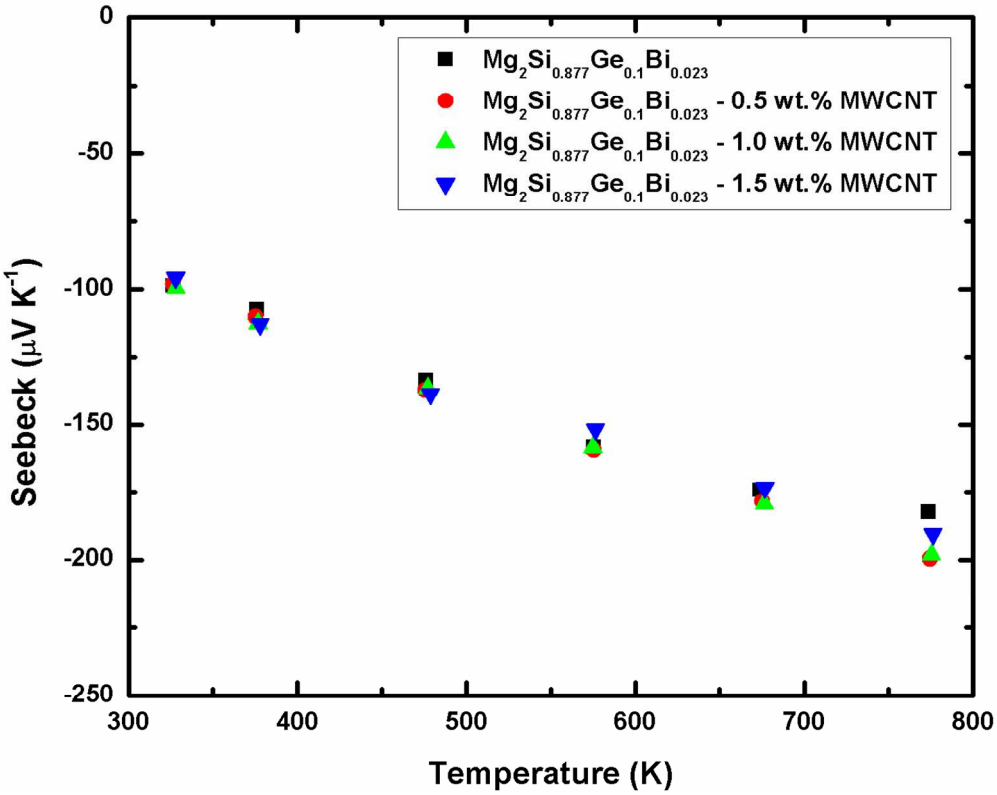

Fig. 8 Seebeck coefficient of the Mg2Si0.877Ge0.1Bi0.023/MWCNT samples.
125x99mm (300 x 300 DPI)

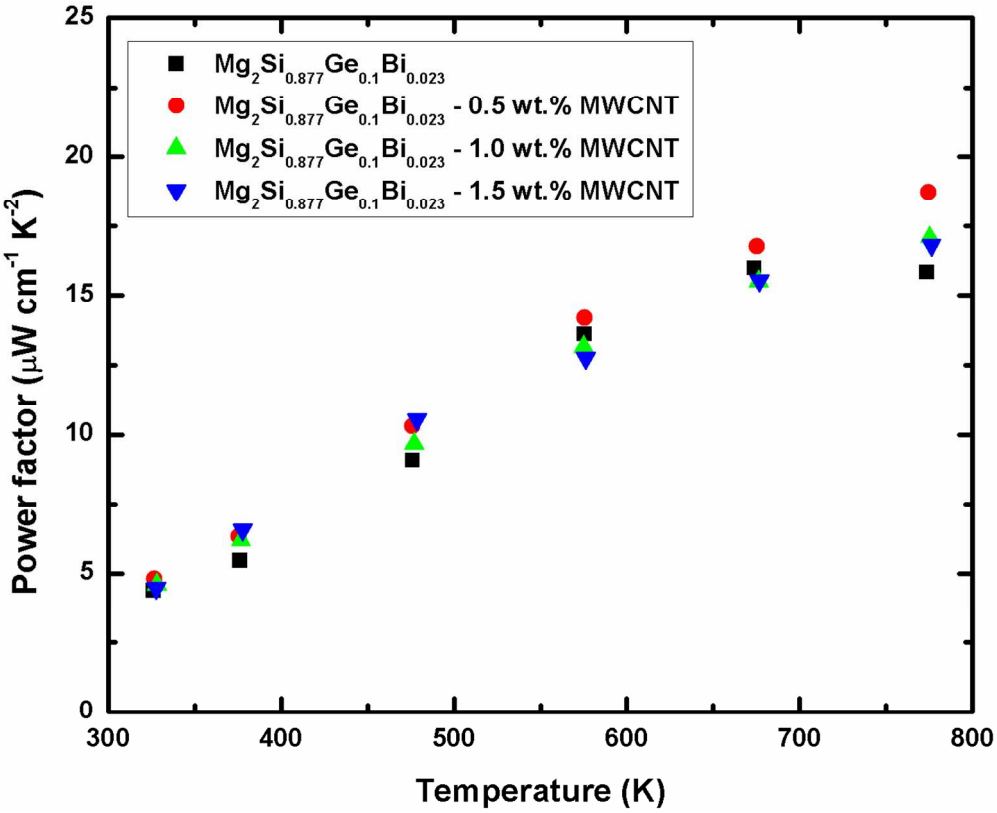

Fig. 9 Power factor of MWCNT/Mg2Si0.877Ge0.1Bi0.023 samples.
122x99mm (300 x 300 DPI)

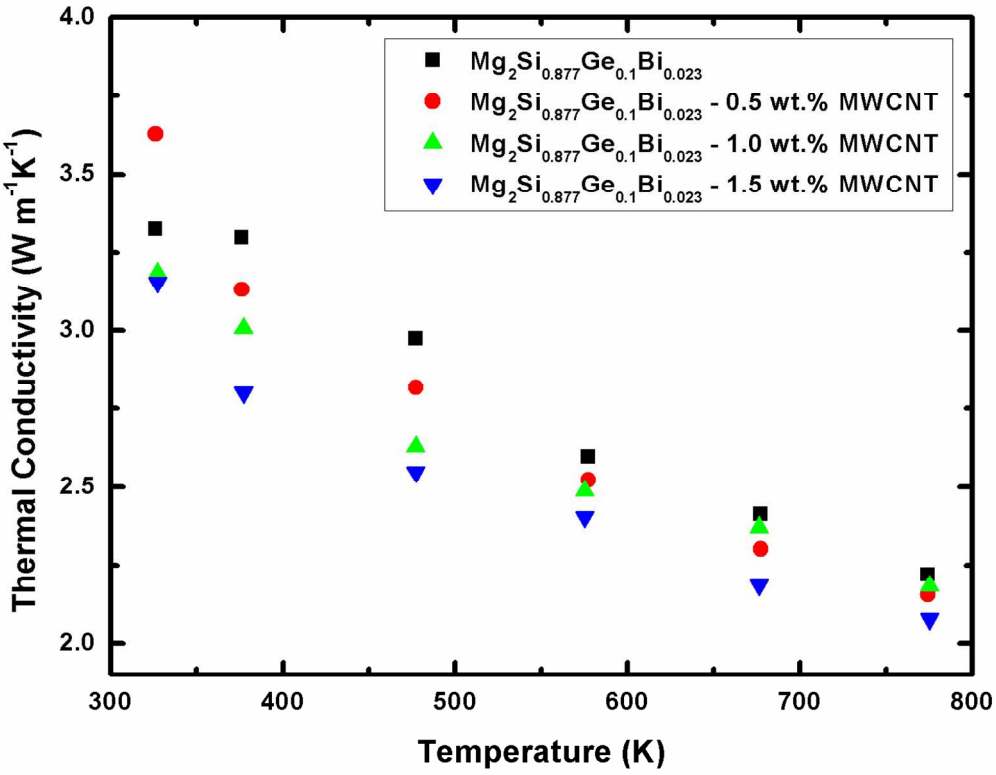

Fig. 10 Thermal conductivity of the Mg2Si0.877Ge0.1Bi0.023/MWCNT samples.
128x99mm (300 x 300 DPI)

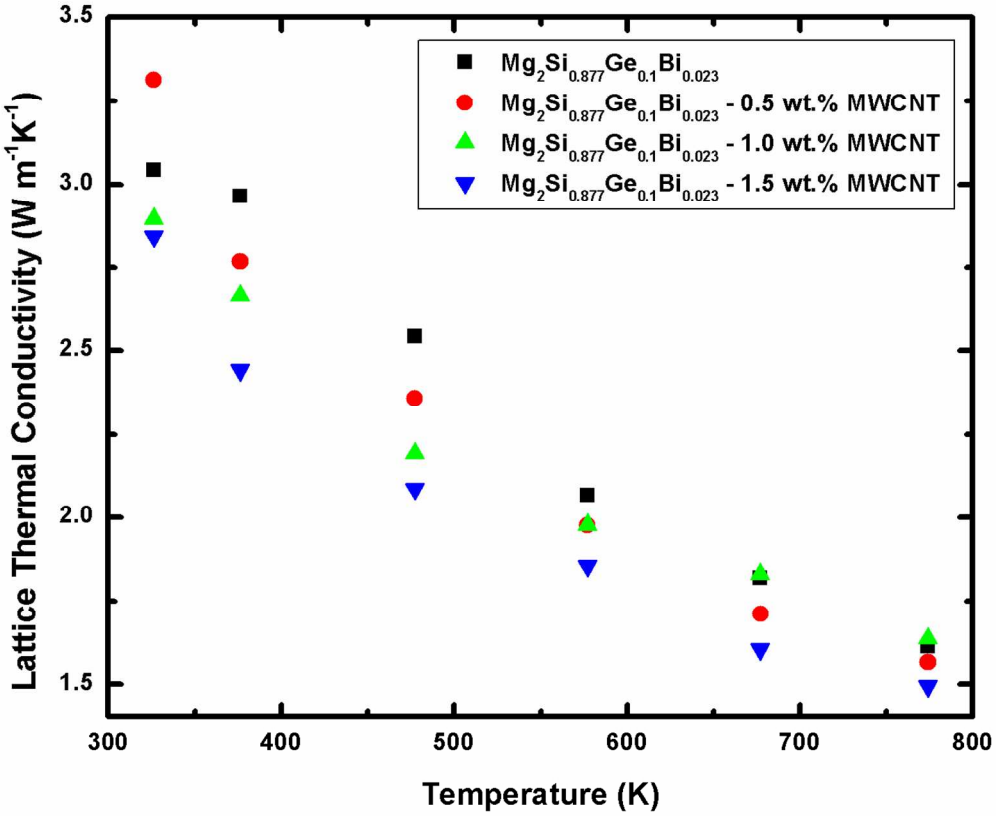

Fig. 11 Lattice thermal conductivity of the Mg2Si0.877Ge0.1Bi0.023/MWCNT samples.
121x99mm (300 x 300 DPI)

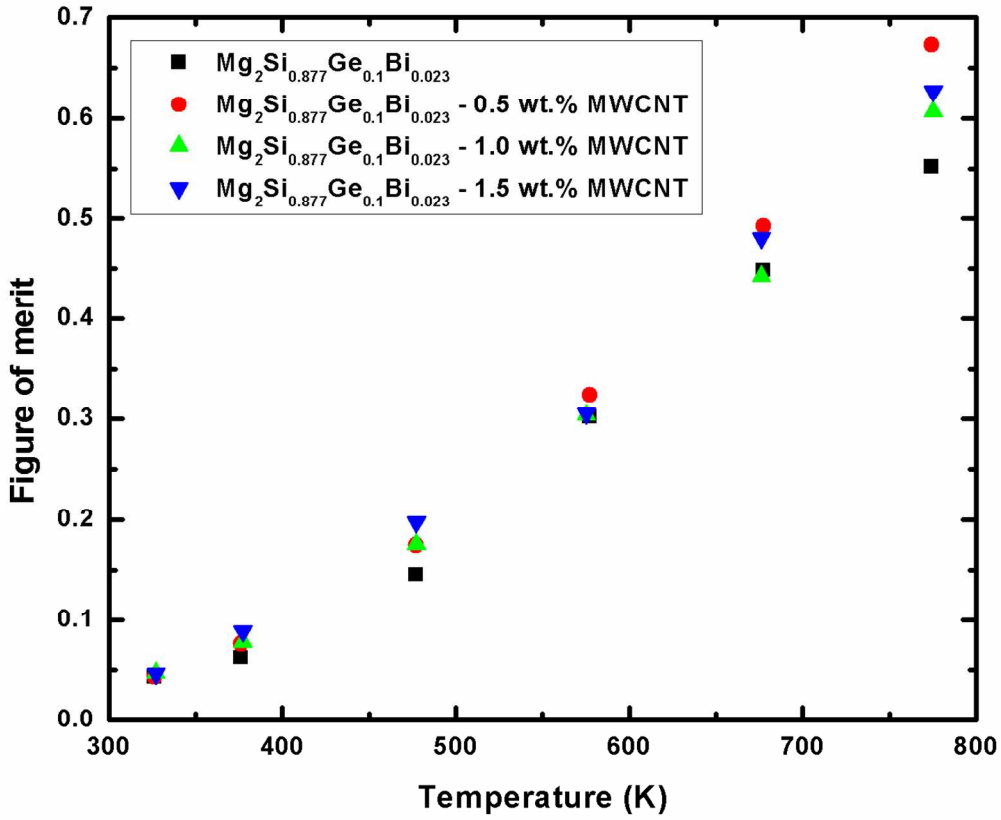

Fig. 12 Figure of merit of the Mg2Si0.877Ge0.1Bi0.023/MWCNT samples.
121x99mm (300 x 300 DPI)